RESEARCH ARTICLE
SOLID EARTH: GEOELECTROMAGNETICS

Earth and Planetary Physics
9: 667–676, 2025
doi: 10.26464/epp2025058

A 100-degree lithospheric magnetic field model constructed using MSS-1, Swarm-A, and CHAMP satellite data

JiaXuan Zhang[1,2,3,4], Yan Feng[1,2,3*], Pan Zhang[5], YuXuan Lin[1,2,3], XinWu Li[1,2,3], and Ya Huang[2]

[1]Institute of Space Weather, School of Atmospheric Physics, Nanjing University of Information Science & Technology, Nanjing 210044, China;

[2]State Key Laboratory of Space Weather, Chinese Academy of Sciences, Beijing 100190, China;

[3]State Key Laboratory of Environment Characteristics and Effects for Near-space, Nanjing University of Information Science & Technology, Nanjing 210044, China;

[4]Macau Institute of Space Technology and Application, Macau University of Science and Technology, Macao 999078, China;

[5]Hubei Subsurface Multi-scale Imaging Key Laboratory, School of Geophysics and Geomatics, China University of Geosciences, Wuhan 430074, China

Key Points:

- We present the first lithospheric magnetic field model based on data from the Macau Science Satellite-1 (MSS-1), Swarm-A, and Challenging Minisatellite Payload (CHAMP) missions.
- The line-leveling technique is used to reduce offsets between adjacent orbital tracks.
- Track-by-track filtering and singular spectrum analysis assist in removing nonlithospheric signals.

Citation: Zhang, J. X., Feng, Y., Zhang, P., Lin, Y. X., Li, X. W., and Huang Y. (2025). A 100-degree lithospheric magnetic field model constructed using MSS-1, Swarm-A, and CHAMP satellite data. *Earth Planet. Phys.*, *9*(3), 667–676. http://doi.org/10.26464/epp2025058

Abstract: By combining data from the Challenging Minisatellite Payload (CHAMP), Swarm-A, and newest Macau Science Satellite-1 (MSS-1) missions, we constructed a lithospheric magnetic field model up to spherical harmonic degree $N = 100$. To isolate the lithospheric magnetic field signals, we utilized the latest CHAOS-8 (CHAMP, Ørsted, and SAC-C 8) model and MGFM (Multisource Geomagnetic Field Model) to remove nonlithospheric sources, including the core field, magnetospheric field, ocean tidal field, and ocean circulation field. Subsequently, orbit-by-orbit processing was applied to both scalar and vector data, such as spherical harmonic high-pass filtering, singular spectrum analysis, and line leveling, to suppress noise and residual signals along the satellite tracks. With an orbital inclination of only 41°, MSS-1 effectively captures fine-scale lithospheric magnetic field signals in mid- to low-latitude regions. Its data exhibit a root mean square error of only 0.77 nT relative to the final model, confirming the high quality and utility of lithospheric field modeling. The resulting model exhibits excellent consistency with the MF7 (Magnetic Field Model 7), maintaining a high correlation up to $N = 90$ and still exceeding 0.65 at $N = 100$. These results demonstrate the reliability and value of MSS-1 data in global lithospheric magnetic field modeling.

Keywords: lithospheric magnetic field; Macau Science Satellite-1 (MSS-1); line leveling; Magnetic Field Model 7 (MF7); singular spectrum analysis

1. Introduction

The geomagnetic field is a superposition of magnetic fields from various sources, among which the lithospheric magnetic field, generated by magnetized rocks in the Earth's crust, constitutes a crucial component. It is one of the weakest magnetic fields detectable by low earth orbit satellites, and it plays an essential role in natural resource exploration and geomagnetic navigation (Thébault et al., 2010). The lithospheric field is nearly time invariant within a time scale of approximately 17 years at satellite altitude (Sebera et al., 2019). Comprehensive characterization requires dense spatial measurements, for which precise, globally distributed satellite observations are undoubtedly the optimal choice (Olsen et al., 2017).

The launches of the Ørsted (Neubert et al., 2001), CHAMP (Challenging Minisatellite Payload; Reigber et al., 2002), and SAC-C (Satélite de Aplicaciones Científicas-C) satellites from 1999 onward provided much high-precision data for lithospheric field modeling, leading to the development of magnetic field models such as the MF (Magnetic Field Model) series (Maus et al., 2006, 2007), the CHAOS (CHAMP, Ørsted, and SAC-C) series (Olsen et al., 2006; Finlay et al., 2020), the CM (Comprehensive Model) series (Sabaka et al., 2015, 2020), and the NGDC-720 (National Geophysical Data Center's degree 720 magnetic model; Maus, 2010). The Swarm constellation, launched by the European Space Agency in 2013 (Friis-Christensen et al., 2006), provides high-precision magnetic field measurements. Its unique dual-satellite side-by-

First author: J. X. Zhang, zhangjiaxuan2022@outlook.com
Correspondence to: Y. Feng, frank_feng8848@163.com
Received 27 DEC 2024; Accepted 03 APR 2025.
First Published online 28 APR 2025.

side configuration enables the generation of gradient data, which has been used to develop several high-quality lithospheric magnetic field models (Olsen et al., 2017; Thébault et al., 2021).

The Macau Science Satellite-1 (MSS-1), the newest geomagnetic satellite that launched on May 21, 2023, is a low-inclination orbital mission designed to study the spatiotemporal variations of the Earth's magnetic field, particularly in the mid- to low-latitude regions and the South Atlantic Anomaly (Zhang K, 2023). Operating at an altitude of approximately 450 km with an orbital inclination of about 41°, the satellite is equipped with an optical platform and high-precision magnetometers, similar to those on the Swarm satellites, enabling the acquisition of accurate magnetic field data (Yan Q et al., 2023). The combination of MSS-1 and Swarm satellite data has resulted in the MSS-1 Initial Field Model (MIFM; Jiang Y et al., 2024), demonstrating the high quality of MSS-1 data and its potential for integration with Swarm satellite observations.

The lithospheric magnetic field, a significant component of the geomagnetic field, can be modeled using two principal approaches (Thébault et al., 2010). The first is comprehensive inversion, such as in the CHAOS-7 model (Finlay et al., 2020), which uses satellite and observatory data to estimate the core, lithospheric, and magnetospheric fields simultaneously. This approach excels in capturing the combined contributions of major internal and external field sources. However, a key limitation lies in the relatively weak lithospheric field signal, which can be overshadowed by the stronger core and magnetospheric fields. The second approach is sequential inversion, as in the MF6 model (Maus et al., 2008).This method involves using models to subtract contributions from the core, magnetospheric, and ocean tidal fields from the observed data, followed by further processing and modeling. However, not all nonlithospheric field signals can be removed through the premodel subtraction, and unmodeled external fields may still influence lithospheric signals.

In the present study, we utilize sequential inversion methods to develop a lithospheric field model up to spherical harmonic degree (N) 100 based on satellite magnetic field data. To better characterize the global lithospheric field, we incorporate not only CHAMP and Swarm-A measurements but also newly released MSS-1 data covering a 14-month time span, whose 41° low-inclination orbit provides increased coverage in mid-latitude regions.

Section 2 describes the data processing techniques designed to address specific issues in current sequential modeling methods. Section 3 introduces the regularization techniques adopted during the modeling and inversion process, effectively preventing overfitting. Section 4 presents an analysis of the resulting model and compares it with other models. Finally, Section 5 provides a summary of the entire study.

2. Data and Processing

The CHAMP satellite, launched in July 2000 with an orbital inclination of 87.2°, operated at an altitude of approximately 300 km during its final 2 years (September 2008–September 2010), allowing for enhanced detection of lithospheric field signals. The CHAMP satellite data used for modeling in this study correspond to this time period and were previously used in the construction of the CHAOS-4h model (Olsen et al., 2014).

The Swarm satellite constellation, launched in November 2013, consists of three satellites. In this study, we used only the magnetic field data from Swarm-A during the period from January 2014 to December 2024. In addition, scalar and vector data from MSS-1 were used for the period from November 2023 to December 2024. During the selected time periods, both satellites operated at altitudes close to 450 km. To use the data from these two satellites for lithospheric magnetic field modeling, a series of preprocessing steps is required, as illustrated in Figure 1.

2.1 Selecting Data During Geomagnetically Quiet Periods

Under quiet conditions, cleaner geomagnetic signals can be

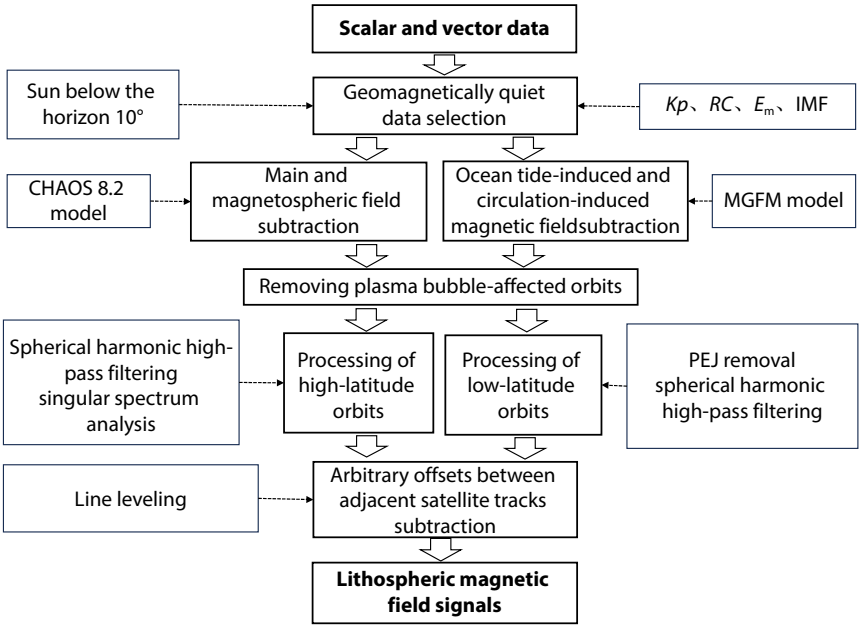

Figure 1. Flowchart of lithospheric magnetic field data processing.

obtained. Following the data selection criteria from the CHAOS-8.2 model, we applied the following standards to select both scalar and vector satellite data:

(1) The solar zenith angle should be at least 10° below the horizon;

(2) The ring current index *RC* should not change by more than 2 nT/hour (Olsen et al., 2015);

(3) The geomagnetic activity index $Kp \leq 2°$;

(4) The 1-minute value of the magnetopause electric field E_m (averaged over the previous 2 hours) ≤ 0.8 mV/m (Newell et al., 2007);

(5) The interplanetary magnetic field (IMF) B_z (averaged over the previous 2 hours) > 0;

(6) For QD (quasi-dipole) latitude > 0, the IMF B_y (averaged over the previous 2 hours) < 3 nT; for QD latitude < 0, the IMF B_y (averaged over the previous 2 hours) > –3 nT.

Considering that ionospheric currents during nighttime are negligible, we did not apply corrections for F-region currents during the quiet period data processing (Maus et al., 2008). Stricter thresholds on E_m and IMF parameters effectively suppress external field contamination and improve model accuracy, at the cost of a substantial reduction in data volume. In contrast, more relaxed thresholds increase data availability but may reduce model reliability (Yao HB et al., 2025a).

2.2 Correcting Nonlithospheric Fields with Prior Models

To obtain clean lithospheric field data, we used prior models to remove contributions from other magnetic field sources. For scalar and vector data collected under geomagnetic quiet conditions, we applied the latest CHAOS-8.2 model to eliminate the core field and large-scale magnetospheric fields, whereas we used the MGFM model to remove the ocean tide-induced field and ocean circulation field (Yao HB et al., 2025b).

2.3 Removing Plasma Bubble-Affected Orbits

To minimize the effects of ionospheric currents, we selected the nightside orbits. However, even after sunset, the equatorial ionosphere can still be influenced by localized plasma instabilities ("plasma bubbles"), which may contaminate orbit data by up to 5 nT (Maus et al., 2006). To address this issue, high-pass filtering with a cutoff period of 30 seconds was applied to automatically detect and remove contaminated orbits (Stolle et al., 2006). For instance, when analyzing the total magnetic field intensity (*F*), orbits with adjacent peaks exceeding 0.25 nT within a 6° latitude window were identified as being affected by plasma bubbles and excluded. This process resulted in the removal of approximately 7% of the orbits.

2.4 Polar Electrojet Correction

The polar electrojet (PEJ) during geomagnetically quiet periods should not be overlooked (Maus et al., 2006). The far-field effects of the PEJ can influence the magnetic field at mid- to low-latitude regions. Therefore, we corrected the PEJ currents within the QD latitude range of ±65° on each orbit.

To model and remove the PEJ-induced magnetic signal, we followed the method of Maus et al. (2006), where the electrojet is represented as a circular horizontal current loop centered around the geomagnetic pole at 110 km altitude, with a mirror image current located 100 km below the surface to simulate induction effects. The magnetic field generated by this configuration is fitted and subtracted along each half-orbit, using a two-step procedure: a nonlinear estimation of the current ring radius, followed by a linear fit to determine the current strength, orientation, and background offset. The field contribution is computed based on the Biot–Savart law, with the magnetic effect expressed as

$$\boldsymbol{B}_{\mathrm{PEJ}}(\boldsymbol{r}) = \frac{\mu_0}{4\pi}\int_C \frac{\boldsymbol{I}\times(\boldsymbol{r}-\boldsymbol{r}')}{|\boldsymbol{r}-\boldsymbol{r}'|^3}\mathrm{d}\boldsymbol{l}', \tag{1}$$

where $\boldsymbol{r}$ is the field point, $\boldsymbol{r}'$ is the position on the current loop C, $\boldsymbol{I}$ is the current element vector, $\mathrm{d}\boldsymbol{l}'$ is the differential element along the loop, and $\mu_0 = 4\pi\times10^{-7}$ H/m is the magnetic permeability of free space. This method ensures that the synthetic current system lies outside the observed data region, minimizing the risk of removing true lithospheric signals.

2.5 Spherical Harmonic High-Pass Filtering

According to Kotsiaros et al. (2015), the lithospheric field model constructed using CHAMP satellite gradient data shows an upward trend in the power spectrum beyond degree 80, whereas its correlation with the MF7 and CM5 models decreases significantly at higher degrees. Consequently, we considered satellite-derived data to be reliable for determining spherical harmonic components up to degree 80. Signals beyond degree 80, however, will be the primary focus of our subsequent analysis. For this purpose, we adopted the first 80 degrees of the LCS-1 (Lithospheric model derived from CHAMP and Swarm satellite data-1) model as a reference. The LCS-1 model, constructed using gradient data from CHAMP and the Swarm-A and Swarm-C satellites, demonstrates excellent consistency with the MF7 model and Australian aeromagnetic data. Therefore, it is both reasonable and reliable to use LCS-1 (up to degree 80) to represent the large-scale lithospheric field. The residuals after subtracting this reference field primarily contain fine-scale lithospheric signals, corresponding to the high-degree components ($N > 80$) of the lithospheric magnetic field, which are the focus of this study. These residuals were then used for subsequent procedures, such as along-track filtering and singular spectrum analysis (SSA).

The noise between orbits is primarily caused by unmodeled magnetospheric currents and their induced fields, which are mainly long-wavelength signals. These can be mitigated by using an along-track spherical harmonic high-pass filtering method (Maus et al., 2007). To implement spherical harmonic high-pass filtering, we first subtracted the degree-80 component of the LCS-1 model from the scalar and vector data along each satellite orbit. The resulting residuals, which primarily contain small-scale lithospheric signals and noise, were then used to fit and remove a low-degree spherical harmonic model, thereby isolating the high-frequency signal. As shown in Equation (2), this model describes the magnetic potential field truncated at spherical harmonic degree 1 for both internal and external components, and it includes three internal and three external parameters (Maus et al., 2006). Finally, the degree-80 portion of the LCS-1 model is added back to restore the large-scale lithospheric field content.

$$V(r,\theta,\phi) = a\left(\frac{a}{r}\right)^2 \sum_{m=-1}^{1} g_1^m Y_1^m(\theta,\phi) + a\left(\frac{r}{a}\right) \sum_{m=-1}^{1} q_1^m Y_1^m(\theta,\phi). \quad (2)$$

In Equation (2), $V(r,\theta,\phi)$ is the magnetic scalar potential at geocentric coordinates (r,θ,ϕ), where r is the radial distance, θ is the colatitude, and ϕ is the longitude. The constant a = 6371.2 km is the Earth's reference radius. The first term represents the internal field using degree-1 Gauss coefficients g_1^m, and the second term describes the external field using coefficients q_1^m. The functions $Y_1^m(\theta,\phi)$ are the Schmidt semi-normalized spherical harmonics of degree 1 and order m = –1, 0, 1. Although higher degree spherical harmonic models can more effectively filter out invalid low-frequency signals, they should be applied cautiously, as they may also suppress lithospheric signals (Maus et al., 2006; Thébault et al., 2017).

Taking the descending tracks over the Bangui region in Africa as an example, we illustrate the effects of each data processing step in Figure 2. The removal of PEJ currents (red dots) reduces large-scale disturbances and reveals clearer lithospheric signals. Along-track filtering (yellow) further suppresses residual high-frequency noise and improves the consistency with the LCS-1 model. Notably, the filtering effect displays a north–south asymmetry, with significantly greater stability observed in the northern hemisphere compared with the southern hemisphere. This asymmetry may be attributed to the influence of polar currents.

2.6 Singular Spectrum Analysis

In the polar regions, numerous intersecting and overlapping half-orbits lead to dense sampling, and the presence of strong external sources, such as field-aligned currents and auroral electrojets, introduces additional unmodeled disturbances. To mitigate these effects and enhance the clarity of the lithospheric signal, we applied SSA as a filtering method specifically for polar data (Thébault et al., 2016). We assumed that the first two principal components were disturbance fields and were subsequently removed. It is important to note that if the disturbance field is too weak, this filtering method may unintentionally suppress real lithospheric field signals. To minimize such risks, this processing was exclusively applied to data from the polar regions (Thébault et al., 2017).

2.7 Line Leveling

We applied line leveling methods with the primary goal of minimizing the discrepancies between adjacent orbits to reduce arbitrary offsets (Maus et al., 2006). Our approach conservatively minimizes the weighted residuals between the nearest measurements of orbit pairs and the LCS-1 model (up to degree 110). First, we used a degree-1 internal source field and a degree-3 external source field spherical harmonic correction to adjust the scalar data sets from three latitude ranges (the north polar, south polar, and mid-latitude regions) to each other (Maus et al., 2006). The latitude division is similar to that of MF4, with the region between QD latitude ±65° considered mid-latitude and regions outside QD

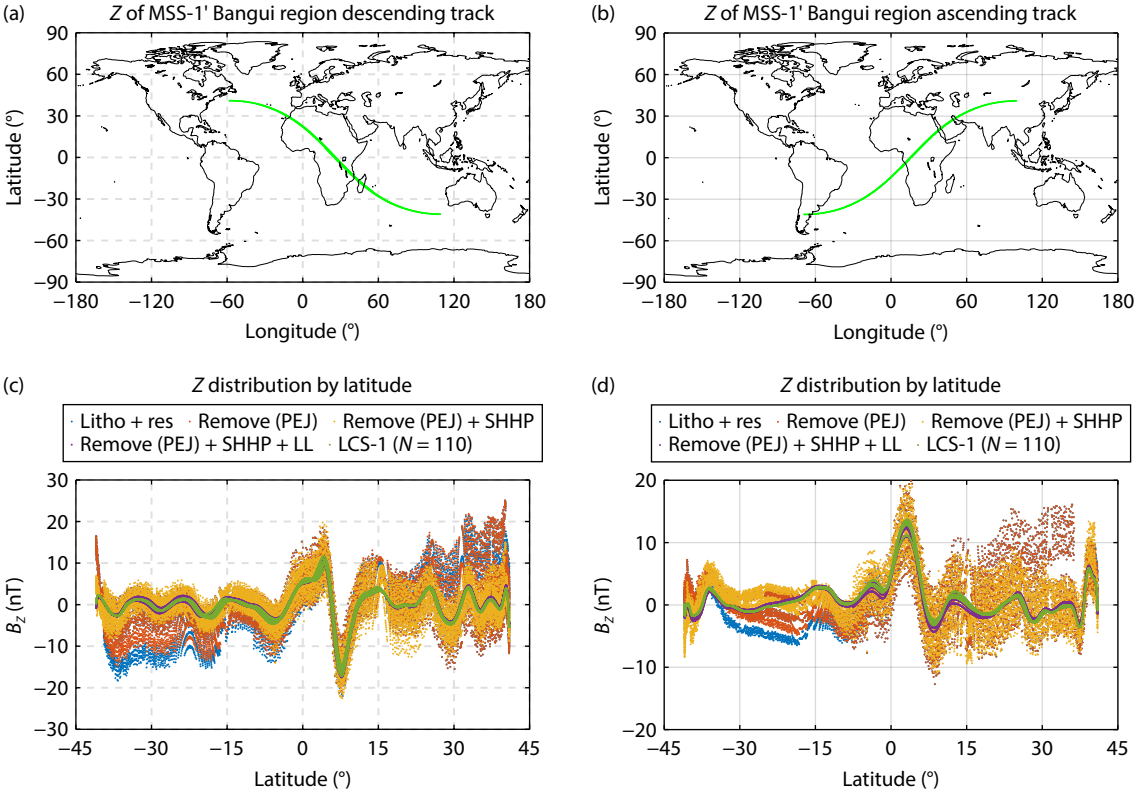

Figure 2. (a) Geographic location of the descending MSS-1 satellite track over the Bangui region of Africa; (b) geographic location of the ascending track; (c) component Z (B_Z) along the descending track after each successive correction step, including PEJ removal, spherical harmonic high-pass filtering (SHHP) filtering, and line leveling (LL); (d) same as (c), but for the ascending track. The LCS-1 model (up to degree 110) is included as a reference.

latitude ±55° classified as polar regions. Subsequently, the same spherical harmonic degrees were applied to adjust the vector data, ensuring consistency with the scalar data. In constructing the spherical harmonic model, vertical distances were weighted according to the weighting function provided in Equation (1) of MF4 (Maus et al., 2006).

The corrected model results and the orbit-by-orbit processed component *Z* of the MSS-1 satellite are shown in Figures 3a and 3c, respectively, whereas the *Z* of the Swarm-A satellite is presented in Figures 3b and 3d. As shown in Figures 3b and 3d, after we applied spherical harmonic high-pass filtering, SSA, PEJ removal, and line leveling, the noise in the data was significantly reduced, resulting in a more refined and smoother representation of lithospheric magnetic anomalies in the satellite data. Meanwhile, fine-scale lithospheric magnetic signals were clearly revealed, particularly in the polar regions.

Application of the line-leveling method is associated with certain challenges. Because it relies on a large number of satellite orbit crossovers, it is more effective in the polar regions than in the mid-latitude areas, where such crossovers are relatively scarce because of the near-polar orbital geometry (Thébault et al., 2017). Therefore, in our modeling process, we chose to apply line-leveling corrections only in the polar regions (|QD latitude| > 55°), whereas for the mid-latitude regions (|QD latitude| ≤ 55°), we retained the original correction scheme based on PEJ removal combined with spherical harmonic high-pass filtering.

2.8 Data Sparsification

To reduce data redundancy caused by closely spaced measurement pairs along each orbital track, we applied a two-step grid-based thinning approach. First, a KD-tree (k-dimensional tree) search was used to map the satellite data points onto a 0.25° × 0.25° grid, retaining only the first-in point assigned to each grid cell. The dataset was then further thinned to a coarser 0.4° × 0.4° grid. This sparsification process was designed to reduce data density and ensure more uniform global coverage. The final data volume used for modeling is presented in Figure 4.

The CHAMP vector data from September 2008 to September 2010 and the Swarm-A vector data from January 2014 to December 2024 were selected within QD latitudes of ±55°. The MSS-1 vector data, covering the period from November 2023 to December 2024, were selected within geographic latitudes of ±41°. The scalar data were selected globally in this study. Notably, Swarm-A had no available data from July to December 2019.

Additionally, to avoid ringing at the poles (Olsen et al., 2014), we used the first 80 degrees of the LCS-1 model to generate a total of 1800 scalar and vector data points located beyond ±87.3° latitude (Olsen et al., 2017). These model-generated data were then combined with CHAMP, Swarm-A, and MSS-1 satellite data for subsequent modeling. Because the model was constructed using data from three satellites, we decided to name it $\mathrm{MODEL_{MSC}}$, where M stands for MSS-1, S represents Swarm-A, and C refers to CHAMP.

3. Modeling Methods

The lithospheric field is generally considered to represent the constant and invariant component of the internal field, assuming that the sampled regional data are not influenced by ionospheric currents, unmodeled induced currents, and the like (Kunagu et al., 2013). Under the geocentric Earth-fixed coordinate system, the magnetic field vector can be expressed as

$$\boldsymbol{B}_{\mathrm{mod}} = \begin{bmatrix} X \\ Y \\ Z \end{bmatrix} = \begin{bmatrix} -B_\theta \\ +B_\phi \\ -B_r \end{bmatrix} = -\nabla V, \tag{3}$$

where *V* is the magnetic scalar potential, which satisfies the

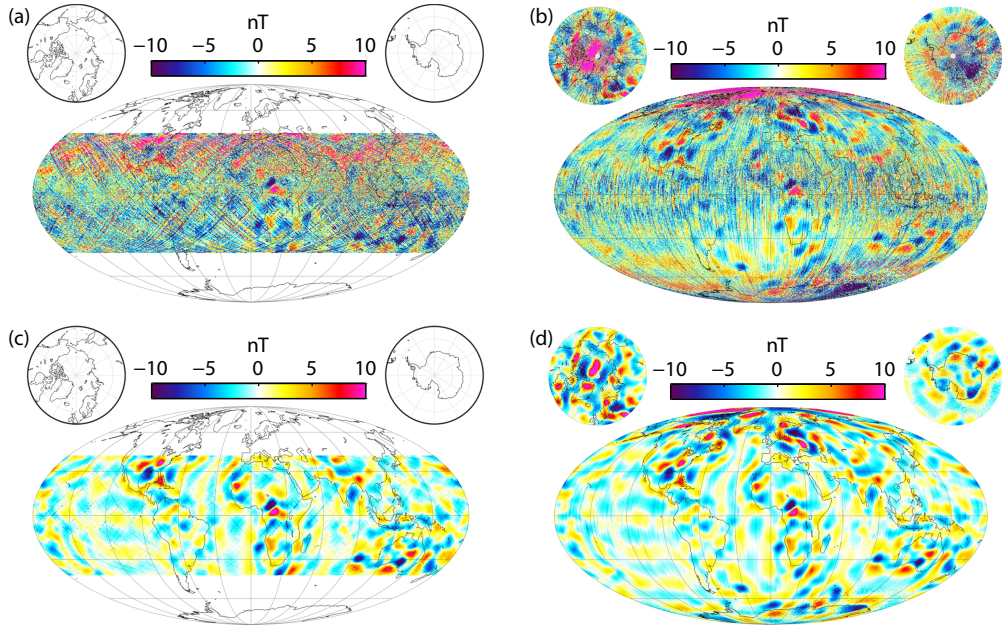

Figure 3. (a) Component *Z* before the processing of MSS-1 satellite data; (b) component *Z* before the processing of Swarm-A satellite data; (c) component *Z* after the processing of MSS-1 satellite data; (d) component *Z* after the processing of Swarm-A satellite data.

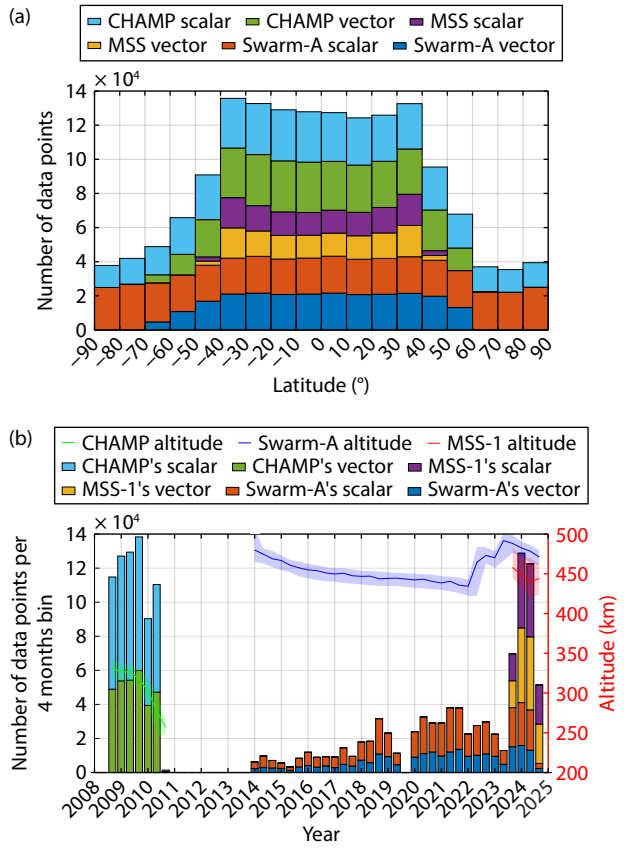

Figure 4. (a) The distribution of satellite data with respect to geographic latitude; (b) the amount of data selected from different satellites and its distribution over time.

Laplace equation and can thus be represented by using a spherical harmonic expansion. In this study, we consider only the internal field, in which case the expression for V is

$$V(r,\theta,\phi) = a\sum_{n=1}^{N_{\rm int}}\sum_{m=0}^{n}\left(\frac{a}{r}\right)^{n+1}\left[g_n^m\cos(m\phi)+h_n^m\sin(m\phi)\right]P_n^m(\cos\theta). \quad (4)$$

Here, P_n^m represents the Schmidt seminormalized associated Legendre functions; $\{g_n^m, h_n^m\}$ are the Gauss coefficients used to describe the internal sources; and $N_{\rm int}$ represents the maximum degree of the expansion. In this study, we truncate the lithospheric field at $N_{\rm int}$ = 100, resulting in a total of 10,200 Gauss coefficients.

To estimate the model parameters $\boldsymbol{x} = \{g_n^m, h_n^m\}$ from satellite data, we utilize the least squares method to solve the linear equation:

$$\boldsymbol{Ax} = \boldsymbol{b}. \quad (5)$$

Here, $\boldsymbol{x}$ is the model vector, $\boldsymbol{b}$ is the data vector, and $\boldsymbol{A}$ is the kernel matrix. The objective is to minimize the sum of squares of the residual vector $\boldsymbol{e} = \boldsymbol{b}_{\rm obs} - \boldsymbol{b}_{\rm mod}$. However, because the data used in the modeling also contain unmodeled external fields, $\rm MODEL_{MSC}$ is incomplete, and the residuals do not follow a Gaussian distribution (Walker and Jackson, 2000). Therefore, the results obtained directly through standard least squares methods are not reliable. For example, when testing the least squares estimation using Swarm satellite data, the results exhibit behavior similar to the SIFM (Swarm Initial Field Model) no-gradient model (Olsen et al., 2015). Coefficients up to degree 40 show stable variations, whereas higher degree coefficients often exhibit a "blow-up" in their power spectra, and noise contamination and overfitting during the solving process may contribute to this instability.

To better fit the satellite data, we used an iteratively reweighted least squares (IRLS) method with regularization for solving the problem:

$$\boldsymbol{x} = (\boldsymbol{A}^{\rm T}\boldsymbol{W}_d^{\rm T}\boldsymbol{W}_d\boldsymbol{A} + \lambda\boldsymbol{I})^{-1}\boldsymbol{A}^{\rm T}\boldsymbol{W}_d^{\rm T}\boldsymbol{W}_d\boldsymbol{b}. \quad (6)$$

Here, λ is the regularization parameter, $\boldsymbol{I}$ is the identity matrix, and $\boldsymbol{W}_d$ is the diagonal matrix of data weights:

$$\boldsymbol{W}_d = \mathrm{diag}\left(\frac{\sin\theta}{\sigma_i}\right). \quad (7)$$

In the formula, σ_i represents the standard deviation of the ith data point and θ is the colatitude of the data point in the spherical coordinate system. By multiplying $\sin\theta$, we simulate an equal-area distribution, which helps prevent overfitting in data-dense regions during the inversion process.

4. Results and Discussion

We tested different datasets to estimate the model, including using only the low-altitude CHAMP dataset ($\rm MODEL_C$), combining CHAMP with Swarm-A data ($\rm MODEL_{SC}$), using only MSS-1 and Swarm-A data ($\rm MODEL_{SM}$), and adding MSS-1 data to those of CHAMP and Swarm-A ($\rm MODEL_{MSC}$). For all models, we incorporated 1800 scalar and vector data points from the polar regions, generated using the LCS-1 model.

When constructing models using satellite scalar and vector magnetic field data, an unavoidable issue arises: how to evaluate the reliability of the derived model across different spherical harmonic degrees. For degrees $N \leq 60$, the power spectrum of the model closely resembled those of existing models such as MF7 and LCS-1, indicating that the model is stable and reliable within this degree range. However, at higher degrees, such as those beyond degree 60 in the SIFM no-gradient model (Olsen et al., 2015), the power spectrum exhibits an upward trend. This phenomenon is typically attributed to overfitting and can be mitigated through regularization methods. This type of regularization has been widely used in models such as CHAOS-4h.

We chose to adjust the regularization parameter to modify the model, ensuring that the power spectrum of the model appeared stable. For this step, we applied different regularization coefficients to different datasets in Equation (6). Larger coefficients indicate stronger regularization. Starting from 0, we systematically tested various values. After multiple attempts, we determined that the regularization coefficient should be set to 10. The final results, shown in Figure 5a, demonstrate that the model successfully avoids the "instability" phenomenon beyond degree 80.

4.1 Model Residual Statistics

Table 1 presents the total number of data points from different satellites used in model construction, as well as the mean and root mean square (RMS) of the residuals between the observed data and model values. As expected, Swarm-A data, having undergone

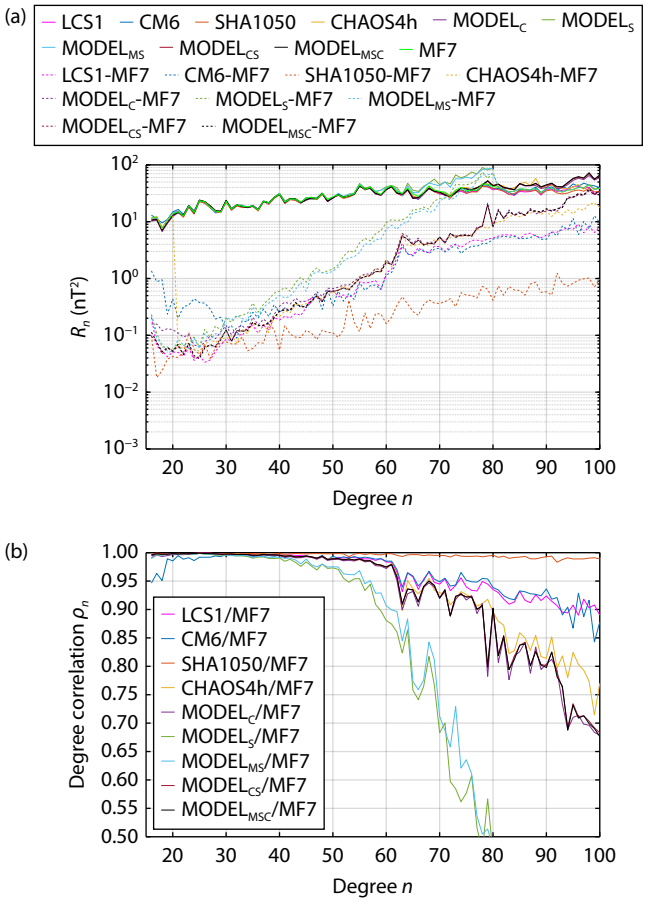

Figure 5. (a) Lowes–Mauersberger power spectrum of various reference and data subset lithospheric field models on the Earth's surface; (b) correlation between various models and the MF7 model. In the model names, M refers to MSS-1, S refers to Swarm-A, and C refers to CHAMP. R_n is lithospheric field power.

stringent selection criteria, show the smallest mean residuals compared to our final model. The larger residuals for CHAMP data may be attributed to the influence of unmodeled ionospheric signals during the selected time period at its lower altitude.

Notably, the overall RMS of the MSS-1 data points is only 0.77 nT. This result highlights the excellent quality of MSS-1 satellite data and its strong capability in representing mid-latitude lithospheric signals.

4.2 Model Comparison

Figure 5a illustrates the power spectra of various versions of the model generated during the modeling process, compared with those of the MF7, CM6, CHAOS-4h, LCS-1, and SHA1050 model (Thébault et al., 2021). In addition to the power spectra of various lithospheric signals, Figure 5a displays the spectral differences between MF7 and other models. The comparison reveals that residual uncertainties remain in lithospheric field modeling. However, the differences between models derived from different methods and datasets are comparatively small. The difference spectra further suggest that current models are reliable up to spherical harmonic degree 80, with relatively small discrepancies extending even to degree 100.

Because we used the same dataset as in the CHAOS-4h model, CHAOS-4h serves as a suitable reference for evaluating the performance of our model. Although CHAOS-8.2 is more recent, its high-degree lithospheric field components are inherited from the LCS-1 model, which is already included in our comparisons.

When examining the model generated using only CHAMP data, CHAOS-4h exhibits a higher energy power spectrum between spherical harmonic degrees $N = 80$ and $N = 90$. In fact, CHAOS-4h shows higher spectral energy within this degree range than other models, including MF7 and LCS-1, as illustrated in Figure 5. However, beyond $n > 85$, regularization is applied, resulting in a steady trend in the power spectrum between degrees 85 and 100. In contrast, the model generated using data from the same time period shows little variation between degrees 80 and 95.

Models generated using both CHAMP and Swarm satellite data, such as CM6 (blue), LCS-1 (magenta), and CHAMP + Swarm-A (brown), exhibit a very similar trend up to degree 90. However, for MODEL$_{MSC}$ and MODEL$_{SC}$, their power spectra begin to rise beyond degree 80, and the differences from MF7 become significantly larger after degree 90. This result indicates that small-scale noise still affects the model signals for spherical harmonic degrees above 90.

Figure 5b illustrates the correlation between different models and the MF7 model. It is evident that models incorporating gradient data, such as CM6, SHA1050, and LCS-1, exhibit higher correlations with MF7. This result highlights the advantages of gradient data because they effectively reduce orbital noise and much of the unmodeled external field contamination. Models such as MF6 and CHAOS-4h, which rely on CHAMP data and regularization, maintain

Table 1. Scalar (F) and vector (X, Y, Z) data point counts (N), mean values (in nanoteslas), and RMS misfit (in nanoteslas) at polar (|QD latitude| > 55°) and nonpolar (|QD latitude| ≤ 55°) latitudes.

Variable	MSS-1			Swarm-A			CHAMP		
	N	Mean	RMS	N	Mean	RMS	N	Mean	RMS
X non-polar	125,546	0.18	0.95	234,630	0.22	0.54	304,060	−0.21	2.49
Y non-polar	125,546	0.03	0.86	234,630	−0.03	1.31	304,060	0.27	2.66
Z non-polar	125,546	−0.04	0.52	234,630	−0.03	0.46	304,060	−0.03	1.59
F non-polar	125,546	0.32	0.69	234,630	0.26	0.54	304,064	−0.42	1.92
F polar	0	0	0	163,952	0.49	0.7	103,532	−0.63	3.33
Total	502,184	0.12	0.77	1,102,472	0.16	0.78	1,319,776	−0.14	2.32

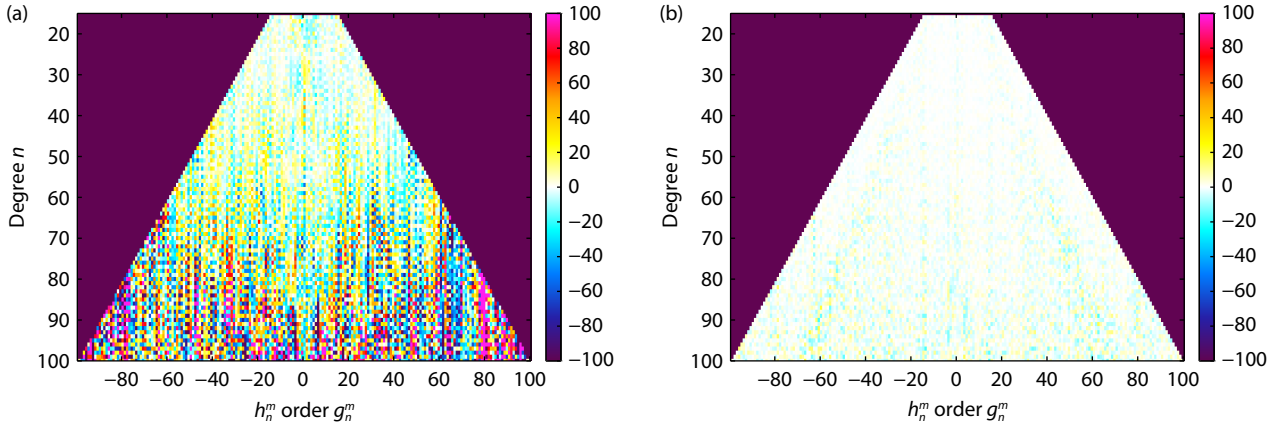

Figure 6. The sensitivity matrix of $MODEL_{MSC}$ differences with respect to the (a) MF7 model coefficients and the (b) $MODEL_{SC}$ coefficients.

correlations above 0.7 for the first 100 degrees. This finding underscores the significant contribution of low-altitude satellites to lithospheric field modeling. We look forward to the launch of the MSS-2 satellite, which is expected to provide additional high-precision data for lithospheric field studies.

As shown comprehensively in Figure 5, the model incorporating MSS-1 data demonstrates improved agreement with the MF7 model. This agreement is clearly evident when comparing $MODEL_S$ and $MODEL_{SM}$. On one hand, MSS-1 provides denser coverage in the mid-latitude regions, offering more observational data for the model; on the other hand, this improvement is also closely related to the high quality of the MSS-1 data.

When combining Figures 5 and 6, we observe that for the first 60 degrees, $MODEL_{MSC}$ exhibits virtually no differences compared to MF7. Up to N = 78, $MODEL_{MSC}$ maintains correlations above 0.9 with MF7, which is also evident in the sensitivity matrix shown in Figure 6. The correlation then gradually decreases, reaching approximately 0.8 at N = 90, and remaining above 0.65 even at N =100.

The inclusion of Swarm-A and MSS-1 data substantially increased vector observations in the mid-latitude regions, contributing to the construction of $MODEL_{MSC}$ and slightly improving its correlation with MF7. Combining this with Figure 6b, the impact of MSS-1 appears limited but is primarily reflected in the spherical harmonic coefficients beyond degree $N > 60$. This finding indicates that MSS-1 data also contribute to the high-degree components of the model.

Overall, the current model shows very small coefficient differences when compared to MF7 and LCS-1. Combining this result with the correlation analysis, we conclude that the spherical harmonic model truncated at degree 90 is highly reliable.

4.3 Global Comparison

Finally, we present the comparison of component Z magnetic field maps generated by different models at the Earth's surface in Figure 7. Figure 7a shows the Z distribution of $MODEL_{MSC}$ at the Earth's surface, highlighting large-scale lithospheric magnetic anomalies. When the details in Figure 7b are compared, the most significant differences are observed in the polar regions. This may be due to the susceptibility of high-latitude regions to disturbances from solar wind particles, which make polar measurements less stable. Despite the application of various processing methods, residual interference from unmodeled external fields may still be present. This may also be attributed to the data processing method, particularly the application of SSA for denoising polar

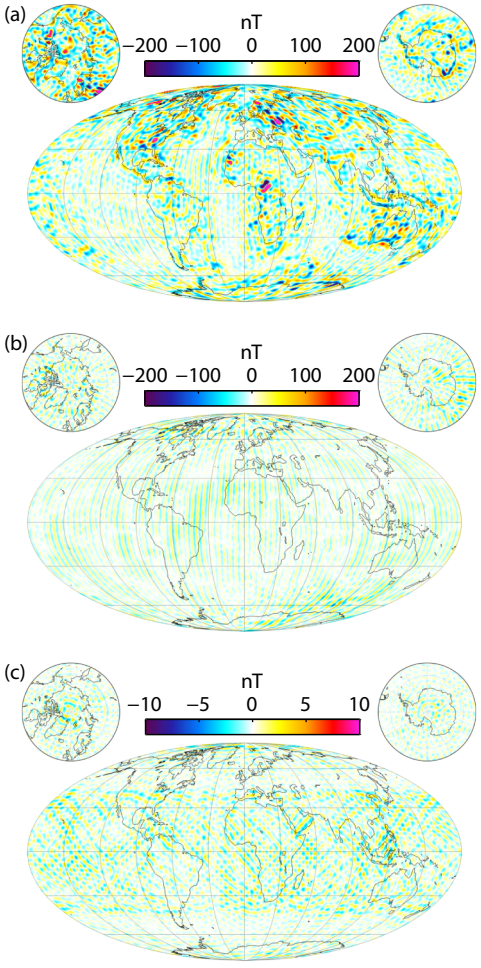

Figure 7. (a) Global surface distribution of component Z from $MODEL_{MSC}$; (b) differences in component Z between $MODEL_{MSC}$ and the MF7 model; (c) differences in component Z with and without MSS-1 data. All values are computed at 0 km altitude (Earth's surface).

observations. Similar patterns have also been reported in previous studies using SSA, such as in the upper panel of Figure 6 in Thébault et al. (2016), suggesting that this method may introduce subtle artifacts or inconsistencies in the polar regions.

Striping observed in mid-latitude western Africa, as documented in models such as CHAOS-4h and Kotsiaros's model (Kotsiaros et al., 2015), is currently attributed to unmodeled magnetospheric fields influencing measurements at satellite altitudes. Another possibility is that the along-track filtering methods may overly penalize extreme but important magnetic field values along the orbital tracks. We anticipate that incorporating east–west gradient data in future work will improve this issue.

Figure 7c compares results obtained by using only CHAMP and Swarm-A data with those that include MSS-1 satellite data. Although the overall differences are minor, notable variations are evident in the mid-latitude regions covered by MSS-1, including Southeast Asia and central and southern Africa. Pronounced boundary effects are observed along the northern and southern edges of the MSS-1 coverage. These findings underscore the importance of addressing boundary effects during data integration, which is essential to further refine the model.

5. Conclusions

We utilized scalar and vector data from 2 years of CHAMP mission measurements, 10 years of Swarm-A mission measurements, and 14 months of MSS-1 mission measurements, and then developed a degree-100 satellite lithospheric magnetic field model, corresponding to a spatial resolution of approximately 400 km. During the processing of Swarm-A and MSS-1 orbital data, we systematically removed signals from the core field, large-scale magnetospheric field, ocean tidal field, and ocean circulation field by using appropriate models. Next, for each orbit, we applied a series of operations, including removing PEJ currents, eliminating plasma bubble effects, applying spherical harmonic high-pass filtering, conducting an SSA, and applying line leveling, with the aim of extracting fine-scale lithospheric magnetic field signals.

The final $\mathrm{MODEL_{MSC}}$ exhibits correlations exceeding 0.8 with the MF7 model for spherical harmonic degrees up to $N = 90$, and a correlation of 0.65 at $N = 100$. The correlation plots and comparisons of global magnetic anomaly maps from forward modeling indicate that $\mathrm{MODEL_{MSC}}$ is reliable on a global scale, demonstrating that MSS-1 satellite data can be effectively used to construct lithospheric magnetic field models.

The inclusion of MSS-1 satellite data significantly enhanced data coverage in the mid-latitude regions and improved the overall stability of the model's power spectrum. The global distribution of $\mathrm{MODEL_{MSC}}$ shows minimal differences from MF7, with the impact of MSS-1 data primarily evident in the mid- to low-latitude regions, especially along the edge bands around ±41° latitude.

Currently, the MSS-1 data are sufficient to cover the mid-latitude regions, and we anticipate acquiring more data from the mid- to low-latitude regions to create overlapping orbits. This will help us further refine orbital characteristics and adjust interorbit offsets. Because of the unique orbital characteristics of MSS-1, the accumulated LT data will provide valuable insights into the contributions from external magnetic fields. Furthermore, its nearly east–west orbit will allow us to capture gradient data, enhancing model accuracy. At the same time, we also look forward to low-altitude, globally covering MSS-2 satellite data to further enhance the reliability and accuracy of the lithospheric magnetic field model.

Acknowledgments

We acknowledge the support of the National Natural Science Foundation of China (Nos. 42250103, 41974073, and 41404053), the Macau Foundation and the preresearch project of Civil Aerospace Technologies (Nos. D020308 and D020303), which is funded by China's National Space Administration, and the Specialized Research Fund for State Key Laboratories.

Open Research

The Swarm data are available at https://swarm-diss.eo.esa.int/#swarm%2FLevel1b%2FEntire_mission_data%2FMAGx_LR, the CHAMP satellite data can be downloaded from ftp://anonymous@isdcftp.gfz-potsdam.de/champ/, the MSS-1 data are available at https://mss.must.edu.mo/data.html, the CHAOS-4h dataset is available at http://www.spacecenter.dk/files/magnetic-models/CHAOS 4/, the CHAOS-8 is available at http://www.spacecenter.dk/files/magnetic-models/CHAOS 8/, the LCS-1 is available at http://www.spacecenter.dk/files/magnetic-models/LCS-1/, the MF7 is available at https://geomag.colorado.edu/magnetic-field-model-mf7.html, and the NGDC-720 is available at https://geomag.us/models/ngdc720.html.

References

Finlay, C. C., Kloss, C., Olsen, N., Hammer, M. D., Tøffner-Clausen, L., Grayver, A., and Kuvshinov, A. (2020). The CHAOS-7 geomagnetic field model and observed changes in the South Atlantic Anomaly. *Earth Planets Space*, *72*(1), 156. https://doi.org/10.1186/s40623-020-01252-9

Friis-Christensen, E., Lühr, H., and Hulot, G. (2006). *Swarm*: A constellation to study the Earth's magnetic field. *Earth Planets Space*, *58*(4), 351–358. https://doi.org/10.1186/BF03351933

Jiang, Y., Finlay, C. C., Olsen, N., Tøffner-Clausen, L., Yan, Q., and Zhang, K. (2024). Macau Scientific Satellite-1 initial magnetic field model. *Geophys. Res. Lett.*, *51*(22), e2024GL112305. https://doi.org/10.1029/2024GL112305

Kotsiaros, S., Finlay, C. C., and Olsen, N. (2015). Use of along-track magnetic field differences in lithospheric field modelling. *Geophys. J. Int.*, *200*(2), 880–889. https://doi.org/10.1093/gji/ggu431

Kunagu, P., Balasis, G., Lesur, V., Chandrasekhar, E., and Papadimitriou, C. (2013). Wavelet characterization of external magnetic sources as observed by CHAMP satellite: Evidence for unmodelled signals in geomagnetic field models. *Geophys. J. Int.*, *192*(3), 946–950. https://doi.org/10.1093/gji/ggs093

Maus, S., Rother, M., Hemant, K., Stolle, C., Lühr, H., Kuvshinov, A., and Olsen, N. (2006). Earth's lithospheric magnetic field determined to spherical harmonic degree 90 from CHAMP satellite measurements. *Geophys. J. Int.*, *164*(2), 319–330. https://doi.org/10.1111/j.1365-246X.2005.02833.x

Maus, S., Lühr, H., Rother, M., Hemant, K., Balasis, G., Ritter, P., and Stolle, C. (2007). Fifth-generation lithospheric magnetic field model from CHAMP satellite measurements. *Geochem. Geophys. Geosyst.*, *8*(5), Q05013. https://doi.org/10.1029/2006GC001521

Maus, S., Yin, F., Lühr, H., Manoj, C., Rother, M., Rauberg, J., Michaelis, I., Stolle, C., and Müller, R. D. (2008). Resolution of direction of oceanic magnetic lineations by the sixth-generation lithospheric magnetic field model from CHAMP satellite magnetic measurements. *Geochem. Geophys. Geosyst.*, *9*(7), Q07021. https://doi.org/10.1029/2008GC001949

Maus, S. (2010). An ellipsoidal harmonic representation of Earth's lithospheric

magnetic field to degree and order 720. *Geochem. Geophys. Geosyst.*, *11*(6), Q06015. https://doi.org/10.1029/2010GC003026

Neubert, T., Mandea, M., Hulot, G., Von Frese, R., Primdahl, F., Jørgensen, J., Friis-Christensen, E., Stauning, P., Olsen, N., and Risbo, T. (2001). Ørsted satellite captures high-precision geomagnetic field data. *Eos, Trans. Am. Geophys. Union, 82*(7), 81–87. https://doi.org/10.1029/01EO00043

Newell, P. T., Sotirelis, T., Liou, K., Meng, C. I., and Rich, F. J. (2007). A nearly universal solar wind-magnetosphere coupling function inferred from 10 magnetospheric state variables. *J. Geophys. Res.: Space Phys.*, *112*(A1), A01206. https://doi.org/10.1029/2006JA012015

Olsen, N., Lühr, H., Sabaka, T. J., Mandea, M., Rother, M., Tøffner-Clausen, L., and Choi, S. (2006). CHAOS—A model of the Earth's magnetic field derived from CHAMP, Ørsted, and SAC-C magnetic satellite data. *Geophys. J. Int.*, *166*(1), 67–75. https://doi.org/10.1111/j.1365-246X.2006.02959.x

Olsen, N., Lühr, H., Finlay, C. C., Sabaka, T. J., Michaelis, I., Rauberg, J., and Tøffner-Clausen, L. (2014). The CHAOS-4 geomagnetic field model. *Geophys. J. Int.*, *197*(2), 815–827. https://doi.org/10.1093/gji/ggu033

Olsen, N., Hulot, G., Lesur, V., Finlay, C. C., Beggan, C., Chulliat, A., Sabaka, T. J., Floberghagen, R., Friis-Christensen, E., … Vigneron, P. (2015). The Swarm initial field model for the 2014 geomagnetic field. *Geophys. Res. Lett.*, *42*(4), 1092–1098. https://doi.org/10.1002/2014GL062659

Olsen, N., Ravat, D., Finlay, C. C., and Kother, L. K. (2017). LCS-1: A high-resolution global model of the lithospheric magnetic field derived from CHAMP and *Swarm* satellite observations. *Geophys. J. Int.*, *211*(3), 1461–1477. https://doi.org/10.1093/gji/ggx381

Reigber, C., Lühr, H., and Schwintzer, P. (2002). CHAMP mission status. *Adv. Space Res.*, *30*(2), 129–134. https://doi.org/10.1016/S0273-1177(02)00276-4

Sabaka, T. J., Olsen, N., Tyler, R. H., and Kuvshinov, A. (2015). CM5, a pre-*Swarm* comprehensive geomagnetic field model derived from over 12 yr of CHAMP, Ørsted, SAC-C and observatory data. *Geophys. J. Int.*, *200*(3), 1596–1626. https://doi.org/10.1093/gji/ggu493

Sabaka, T. J., Tøffner-Clausen, L., Olsen, N., and Finlay, C. C. (2020). CM6: A comprehensive geomagnetic field model derived from both CHAMP and Swarm satellite observations. *Earth Planets Space*, *72*(1), 80. https://doi.org/10.1186/s40623-020-01210-5

Sebera, J., Haagmans, R., Bakyiev, E., and Bezděk, A. (2019). On the observability of the time-variable lithospheric signal in satellite magnetic data. *Surv. Geophys.*, *40*(5), 1229–1243. https://doi.org/10.1007/s10712-019-09546-8

Stolle, C., Lühr, H., Rother, M., and Balasis, G. (2006). Magnetic signatures of equatorial spread *F* as observed by the CHAMP satellite. *J. Geophys. Res.: Space Phys.*, *111*(A2), A02304. https://doi.org/10.1029/2005JA011184

Thébault, E., Purucker, M., Whaler, K. A., Langlais, B., and Sabaka, T. J. (2010). The magnetic field of the Earth's lithosphere. *Space. Sci. Rev.*, *155*(1), 95–127. https://doi.org/10.1007/s11214-010-9667-6

Thébault, E., Vigneron, P., Langlais, B., and Hulot, G. (2016). A Swarm lithospheric magnetic field model to SH degree 80. *Earth Planets Space, 68*(1), 126. https://doi.org/10.1186/s40623-016-0510-5

Thébault, E., Lesur, V., Kauristie, K., and Shore, R. (2017). Magnetic field data correction in space for modelling the lithospheric magnetic field. *Space Sci. Rev.*, *206*(1-4), 191–223. https://doi.org/10.1007/s11214-016-0309-5

Thébault, E., Hulot, G., Langlais, B., and Vigneron, P. (2021). A spherical harmonic model of Earth's lithospheric magnetic field up to degree 1050. *Geophys. Res. Lett.*, *48*(21), e2021GL095147. https://doi.org/10.1029/2021GL095147

Walker, M. R., and Jackson, A. (2000). Robust modelling of the Earth's magnetic field. *Geophys. J. Int.*, *143*(3), 799–808. https://doi.org/10.1046/j.1365-246X.2000.00274.x

Yan, Q., Ou, J. M., Suo, L., Jiang, Y., and Liu, P. F. (2023). Study on the estimation of Euler angles for Macau Science Satellite-1. *Earth Planet. Phys.*, *7*(1), 144–150. https://doi.org/10.26464/epp2023017

Yao, H. B., Xu, J. Y., Jiang, Y., Yan, Q., Yin, L., and Liu, P. F. (2025a). Influence of different data selection criteria on internal geomagnetic field modeling. *Earth Planet. Phys.*, *9*(3), 541–549. https://doi.org/10.26464/epp2025013

Yao, H. B., Xu, J. Y., Yang, C., Ren, Z. Y., and Zhang, K. (2025b). A multisource geomagnetic field model incorporating ocean circulation-induced magnetic field. *Earth Planet. Phys.*, *9*(3), 550–563. https://doi.org/10.26464/epp2025029

Zhang, K. (2023). A novel geomagnetic satellite constellation: Science and applications. *Earth Planet. Phys.*, *7*(1), 4–21. https://doi.org/10.26464/epp2023019